NANO LETTERS

pubs.acs.org/NanoLett Letter

Probing the Polarization of Low-Energy Excitations in 2D Materials from Atomic Crystals to Nanophotonic Arrays Using Momentum-Resolved Electron Energy Loss Spectroscopy

Andrew W. Rossi, Marc R. Bourgeois, Caleb Walton, and David J. Masiello*

Cite This: *Nano Lett.* 2024, 24, 7748−7756 Read Online

ACCESS | Metrics & More | Article Recommendations | Supporting Information

ABSTRACT: Spectroscopies utilizing free electron beams as probes offer detailed information on the reciprocal-space excitations of 2D materials such as graphene and transition metal dichalcogenide monolayers. Yet, despite the attention paid to such quantum materials, less consideration has been given to the electron-beam characterization of 2D periodic nanostructures such as photonic crystals, metasurfaces, and plasmon arrays, which can exhibit the same lattice and excitation symmetries as their atomic analogues albeit at drastically different length, momentum, and energy scales. Because of their lack of covalent bonding and influence of retarded electromagnetic interactions, important physical distinctions arise that complicate interpretation of scattering signals. Here we present a fully-retarded theoretical framework for describing the inelastic scattering of wide-field electron beams from 2D materials and apply it to investigate the complementarity in sample excitation information gained in the measurement of a honeycomb plasmon array versus angle-resolved optical spectroscopy in comparison to single monolayer graphene.

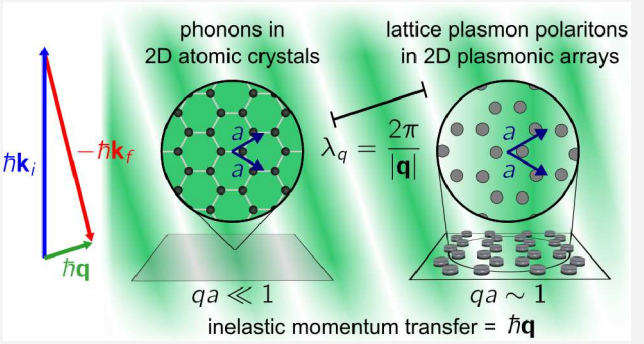

KEYWORDS: *momentum-resolved electron energy loss spectroscopy (q-EELS), high-resolution electron energy loss spectroscopy (HREELS), 2D materials, graphene, plasmon arrays*

Historically, techniques employing low-energy electrons, such as low-energy electron diffraction (LEED), scanning tunneling microscopy (STM), high-resolution electron energy-loss spectroscopy (HREELS), and photoemission spectroscopy (PES), have played a critical role in understanding a range of material properties, from local atomic structure[1−4] to dispersion relations of materials hosting collective excitations.[5−12] The isolation of graphene[13] and other 2D atomic crystals[14−16] has furthered the need for state-of-the-art characterization techniques where the excitonic,[17−20] phononic,[21−26] and plasmonic[27−35] excitations in these materials underlie important applications in optoelectronic devices[18,28,36,37] and quantum information technologies.[38] Due to its atom scale spatial resolution and ability to measure broadband spectral responses, electron energy-loss spectroscopy (EELS) performed inside a scanning transmission electron microscope (STEM) has played an important role in characterizing such 2D materials at their native response scales.[30,39−42] However, the high spatial resolution offered by STEM-EELS relies on momentum space integration, limiting its use as a probe of reciprocal-space excitations. By increasing the incident beam width, parallel beam momentum-resolved EELS (*q*-EELS) in a STEM or wide-field *q*-EELS in a TEM overcomes this challenge, offering sufficient momentum resolution to characterize the dispersive responses of graphene[26,27] and other 2D materials.[17,26,42] Similarly, HREELS[5,23−25,32−35,43,44] and closely related variants[20,31,45] have recently demonstrated the ability to retrieve detailed excitation information on 2D materials.

Like 2D quantum materials, 2D periodic nanophotonic structures, such as photonic crystals, metasurfaces, and plasmon arrays, have been under intense study, owing to their facilely tunable optical properties and role in the formation of new hybrid light−matter states via interaction with excitonic media in both weak and strong coupling regimes. Actively tunable array lasers,[46−49] bound states in the continuum (BICs),[50−56] and exciton−polariton structure, dynamics,[57−62] and room temperature condensation[63,64] represent examples that exploit the energy-momentum dispersion arising from the discrete space translational

Received: April 16, 2024
Revised: June 11, 2024
Accepted: June 12, 2024
Published: June 14, 2024

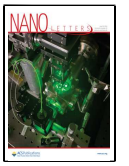

https://doi.org/10.1021/acs.nanolett.4c01797
Nano Lett. 2024, 24, 7748−7756

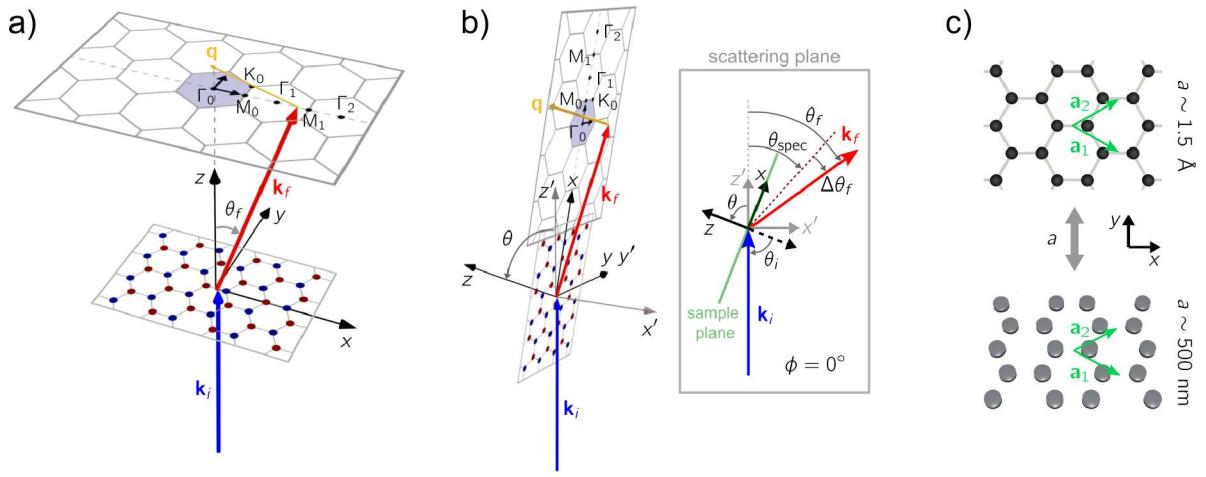

Figure 1. Probing reciprocal-space excitations in 2D material systems with q-EELS. (a) Scheme of q-EELS measurement under forward scattering conditions. Momentum transfers between initial $\mathbf{k}_i$ (blue) and final $\mathbf{k}_f$ (red) free electron states are dictated by the scattering angle θ_f and recoil momentum $\hbar\mathbf{q}$ (yellow) with the projection $\mathbf{q}_\parallel = (\mathbf{q}\cdot\hat{\mathbf{x}})\hat{\mathbf{x}}$ oriented along the Γ−M direction of the sample. (b) Scheme of q-EELS measurement under reflection scattering conditions, otherwise sharing the same kinematical parameters as in transmission. The inset defines the xz-scattering plane relevant to both the transmission and reflection geometries. The detection angle is θ_f in transmission and $\Delta\theta_f = \theta_f - \theta_{spec}$ in reflection, where θ_{spec} is the specular angle. Lab (primed) and sample (unprimed) coordinates are distinguished, and the xz-scattering plane is always perpendicular to the 2D sample xy-plane. Beginning with coincident lab and sample axes as in (a), where only the sample axes are explicitly labeled, and collecting momentum recoils within the $x'z'$-plane, an arbitrary planar scattering configuration can be reached by (i) rotating the sample by angle ϕ about the z'-axis, followed by (ii) rotation by angle θ about the lab y'-axis. (c) Graphene (upper) and a plasmonic array (lower) are examples of 2D periodic honeycomb lattices structured on the atomic and photonic length scales, respectively. a is the magnitude of primitive vectors $\mathbf{a}_1$ and $\mathbf{a}_2$ spanning the real space array. In either case, point M_0 is located at $\mathbf{q}_\parallel = (2\pi/\sqrt{3}\,a, 0)$.

symmetry of the lattice[65,66] to create coherent optical states or simulate complex quantum many-body physics. Measurements of these phenomena necessitate the use of characterization tools with simultaneously high energy, momentum, and polarization resolution. While optical-based probes and cathodoluminescence (CL)[67,68] have been successful in characterizing such materials, the use of q-EELS has been limited to the study of photonic density of states in the vicinity of plasmonic thin film architectures[69] and crystal defects,[70] despite its ability to probe sample excitations with high energy and momentum resolution that are inaccessible to light. Like STEM-EELS, a powerful tool for mapping single nanoparticle excitations,[71−74] momentum-resolved EEL measurements using wide-field electron beams have strong potential in the characterization of periodically structured nanophotonic materials,[75] as exemplified by the routine use of q-EELS and HREELS to interrogate 2D atomic crystals.

Here we present a common theoretical framework for the interpretation of wide-field q-EELS signals in the measurement of the broadband reciprocal-space excitations in 2D periodic materials spanning from atomic to nanoscale and larger dimension. Described within our formalism is the energy-momentum dependence of the probing electron's polarization and relativistic kinematics, additionally illuminating the behavior of reflection scattering processes typical of HREELS across atomic and nanophotonic regimes. While well understood as a probe of 2D materials with angstrom-scale bond lengths, the $\gtrsim$100 nm periodicity scale of 2D nanophotonic materials such as photonic crystals, metasurfaces, and plasmon arrays presents a distinctly new physical regime where electromagnetic retardation effects prevail and companion wide-field inelastic electron scattering observables must be interpreted accordingly. Through the lens of expanded selection rules appropriate to fully retarded light−matter interactions, we elucidate the conditions under which q-EELS can be adapted for measuring the broadband excitations of nanophotonic 2D materials with emphasis placed upon the evolution of the selection rules for scattering processes both within and beyond the first Brillouin zone (BZ), the excitation of optically dark transitions lying off of the light cone, and the role of electron speed and collection geometry. The general complementarity in sample excitation information between wide-field electrons and light is also highlighted. Throughout, contrast and comparison between the IR vibrational excitations of graphene and the optical-frequency excitations of a plasmonic honeycomb lattice are made to illustrate the utility of wide-field EELS in probing 2D materials excitations spanning broadly across disparate spatial, momentum, and energy scales.

The schemes in Figures 1a,b show a pair of generic wide-field inelastic electron scattering events whereby an incoming free electron plane wave with wave vector $\mathbf{k}_i$ (blue) scatters to an outgoing plane wave with wave vector $\mathbf{k}_f$ (red) via interaction with a 2D periodic material sample. The linear momentum $\hbar\mathbf{q} = \hbar(\mathbf{k}_i - \mathbf{k}_f)$ lost by the probing electron is transferred into excited sample states, inducing the transition $|0\rangle \rightarrow |n\rangle$. Experimental conditions, such as detection of transmitted (Figure 1a) versus reflected (Figure 1b) electrons as well as the specific incident and collection angles involved, fix $\mathbf{q}$ (yellow), while the projection $\mathbf{q}_\parallel$ of $\mathbf{q}$ onto the xy sample plane can be manipulated by rotating the sample. Throughout, $\phi = 0°$ such that transverse recoils $\mathbf{q}\cdot\hat{\mathbf{x}}$ in the xz-scattering plane are connected with reciprocal space excitations in the 2D-periodic samples with Bloch vectors $(\mathbf{K}\cdot\hat{\mathbf{x}})\hat{\mathbf{x}}$.

As representative 2D-periodic samples that support reciprocal-space excitations in the low-loss regime, we consider graphene and a plasmonic honeycomb array (Figure 1c), which support phonons and lattice plasmon polaritons (LPPs), respectively. The 2D atomic (nanoparticle) positions $\mathbf{x}_{n\kappa} = \mathbf{x}_n + \mathbf{r}_\kappa = n_1\mathbf{a}_1 + n_2\mathbf{a}_2 + \mathbf{r}_\kappa$ in the graphene (plasmonic array) case are

https://doi.org/10.1021/acs.nanolett.4c01797
Nano Lett. 2024, 24, 7748−7756

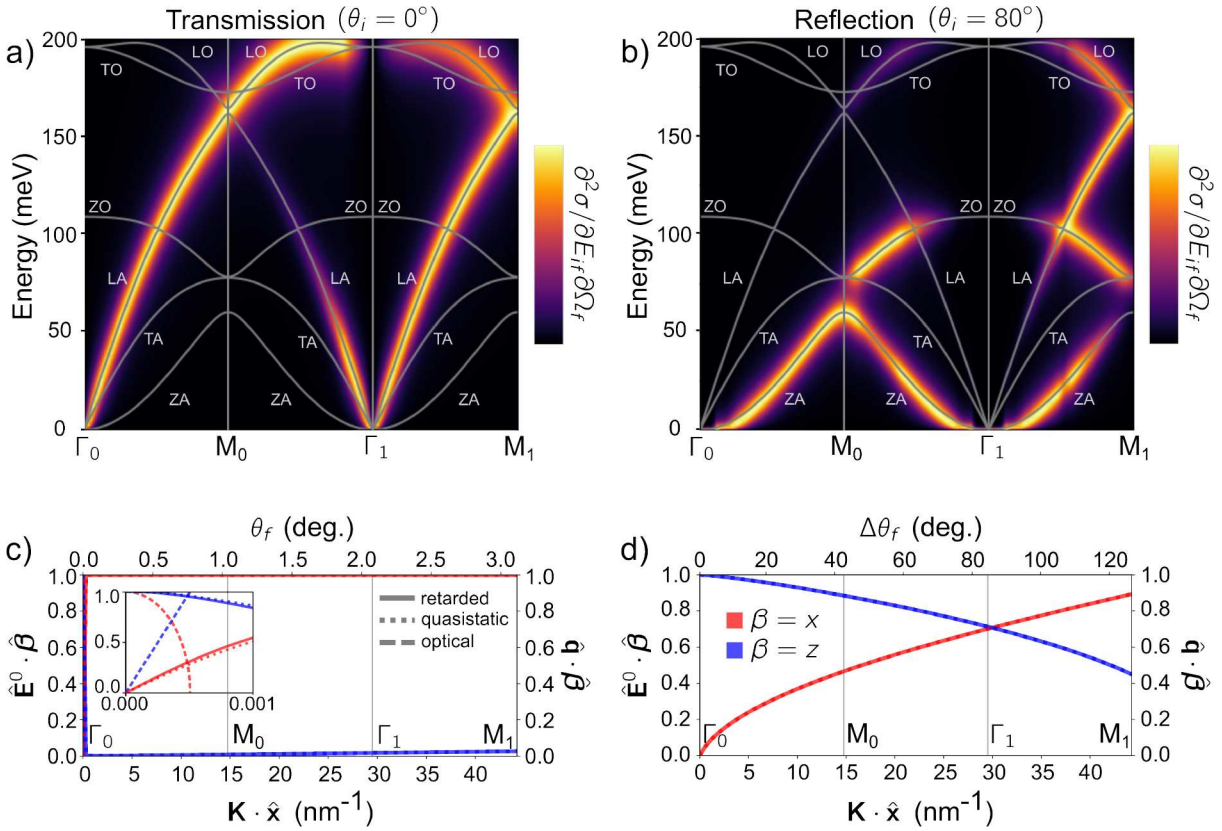

Figure 2. Energy-momentum dispersion of graphene phonons probed along the Γ−M direction. (a) and (b) display the q-EELS DDCS in the transmission and reflection geometries, respectively. Each spectrum at fixed $\mathbf{q}_\parallel$ is independently normalized to the maximum DDCS value at that $\mathbf{q}_\parallel$ point as in ref 26. Gray traces indicate the dispersion of the graphene phonon eigenenergies. (c) and (d) show the normalized magnitude of the in-plane $\mathbf{E}^0_{fi}\cdot\hat{\mathbf{x}}$ (red) and out-of-plane $\mathbf{E}^0_{fi}\cdot\hat{\mathbf{z}}$ (blue) components of the electron's vacuum transition field at E_{if} = 100 meV versus $\mathbf{q}_\parallel$ along Γ_0−M_1, computed in the fully retarded (solid) and quasi-static (dotted) limits in transmission (c) and reflection (d) geometries. Note the scale difference between θ_f and $\Delta\theta_f$ in (c) and (d). The inset in (c) shows the dispersion of $\mathbf{E}^0_{fi}$ as well as that of free space plane wave light $\mathbf{E}^0 = E_0\hat{\boldsymbol{\epsilon}}(\mathbf{k})$ in the immediate vicinity of the Γ_0 point, where the dashed lines represent the in-plane $\mathbf{E}^0\cdot\hat{\mathbf{x}}$ (red) and out-of-plane $\mathbf{E}^0\cdot\hat{\mathbf{z}}$ (blue) components of the incident optical field at $\hbar\omega$ = 100 meV versus in-plane wave vector $\mathbf{k}_\parallel = (\mathbf{k}\cdot\mathbf{x})\hat{\mathbf{x}}$. In (a) and (c), the incident electron wave vector $\mathbf{k}_i$ is oriented normal to the sample plane ($\theta_i = 0°$) with initial velocity $v_i = 0.3c$. In (b) and (d), $\theta_i = 80°$ with respect to the surface normal in the xz-scattering plane and $v_i = 0.01c$. All calculations include an empirical damping rate of η = 20 meV/$\hbar$ at zero temperature and a vacuum background.

situated on a honeycomb lattice, which is a hexagonal Bravais lattice described by primitive lattice vectors $\mathbf{a}_1$ and $\mathbf{a}_2$, with $|\mathbf{a}_1| = |\mathbf{a}_2| = a$ and $s = 2$ sites per unit cell labeled by κ. These sites are colored red and blue in Figures 1a,b. While both honeycomb arrays share common real space and reciprocal space symmetry, the characteristic length scale is a = 1.42 Å for graphene and a = 460 nm for the plasmonic array.

The Hamiltonian involving either class of 2D material can be partitioned as $\hat{H} = \hat{H}_0 + \hat{H}_{\text{int}}$, where $\hat{H}_0 = \hat{H}_s + \hat{H}_{\text{el}}$ is the sum of sample $\hat{H}_s$ and free electron $\hat{H}_{\text{el}}$ components and $\hat{H}_{\text{int}}$ is the interaction Hamiltonian. Beginning from minimal coupling and working in the generalized Coulomb gauge,[76] the interaction Hamiltonian is $\hat{H}_{\text{int}} = (e/2mc)[\hat{\mathbf{A}}\cdot\hat{\mathbf{p}} + \hat{\mathbf{p}}\cdot\hat{\mathbf{A}}]$, where m and $-e$ are the electron mass and charge, and $\hat{\mathbf{A}}$ and $\hat{\mathbf{p}}$ are the quantum mechanical operators associated with the vector potential of the target and the linear momentum of the free electron probe, respectively. The wide-field double differential cross section (DDCS) with fully retarded probe−sample interactions becomes[77,78]

$$\frac{\partial^2\sigma}{\partial E_{if}\,\partial\Omega_f} = \left(\frac{mL^3}{\pi\hbar^2}\right)^2\left(\frac{k_f}{k_i}\right)\int \mathrm{d}\omega\,\mathrm{d}\mathbf{x}\,\mathrm{d}\mathbf{x}' \times \mathrm{Im}[\mathbf{J}^*_{fi}(\mathbf{x})\cdot\bar{\mathbf{G}}(\mathbf{x},\mathbf{x}',\omega)\cdot\mathbf{J}_{fi}(\mathbf{x}')]\delta(\omega - \varepsilon_{if}) \quad (1)$$

where L is the box quantization length, $E_{if} = \hbar\varepsilon_{if} = \hbar\varepsilon_i - \hbar\varepsilon_f$ is the loss energy, and $\hbar\varepsilon_{i/f} = \gamma_{i/f}mc^2$ with initial/final Lorentz contraction factors $\gamma_{i/f} = [1 - (v_{i/f}/c)^2]^{-1/2}$. The transition current density produced as the probing electron transitions between incoming $\psi_i(\mathbf{x}) = L^{-3/2}e^{i\mathbf{k}_i\cdot\mathbf{x}}$ and outgoing $\psi_f(\mathbf{x}) = L^{-3/2}e^{i\mathbf{k}_f\cdot\mathbf{x}}$ plane-wave states is $\mathbf{J}_{fi}(\mathbf{x}) = -(e\hbar/2mL^3)(2\mathbf{k}_i - \mathbf{q})e^{i\,\mathbf{q}\cdot\mathbf{x}}$, while $\bar{\mathbf{G}}(\mathbf{x},\mathbf{x}',\omega)$ is the dyadic Green's tensor characterizing the electromagnetic responses of the sample. Leveraging the plane waveform of $\mathbf{J}_{fi}(\mathbf{x})$, eq 1 can be recast as

$$\frac{\partial^2\sigma}{\partial E_{if}\,\partial\Omega_f} = -\frac{1}{\pi}\left(\frac{mv_iL^2}{2\pi\hbar^2}\right)^2\left(\frac{k_f}{k_i}\right)\sum_{\kappa\kappa'}\mathrm{Im}[\mathbf{E}^{0*}_{fi,\mathbf{q}\kappa}(\varepsilon_{if})\cdot\bar{\mathbf{\Pi}}_{\mathbf{q}\kappa\kappa'}(\varepsilon_{if})\cdot\mathbf{E}^0_{fi,\mathbf{q}\kappa'}(\varepsilon_{if})] = -\frac{1}{\pi}\left(\frac{mv_iL^2}{2\pi\hbar^2}\right)^2\left(\frac{k_f}{k_i}\right)\sum_{\kappa}\mathrm{Im}[\mathbf{E}^{0*}_{fi,\mathbf{q}\kappa}(\varepsilon_{if})\cdot\mathbf{p}_{n0,\mathbf{q}\kappa}(\varepsilon_{if})] \quad (2)$$

where

https://doi.org/10.1021/acs.nanolett.4c01797
Nano Lett. 2024, 24, 7748−7756

$$\mathbf{E}^0_{fi,\mathbf{q}\kappa} = \frac{2\pi i e\gamma_i}{k_i L^2 \omega} \frac{(\omega/c)^2\overline{\mathbf{I}} - \mathbf{qq}}{(\omega/c)^2 - q^2}\cdot(2\mathbf{k}_i - \mathbf{q})e^{i\mathbf{q}\cdot\mathbf{r}_\kappa} \tag{3}$$

is the Fourier coefficient of the probe's vacuum transition field $\mathbf{E}^0_{fi}(\mathbf{x},\omega) = -4\pi i\omega\int d\mathbf{x}'\ \overline{\mathbf{G}}_0(\mathbf{x},\mathbf{x}',\omega)\cdot(L/v_i)\mathbf{J}_{fi}(\mathbf{x}')$ with free space Green's dyadic $\overline{\mathbf{G}}_0(\mathbf{x},\mathbf{x}',\omega) = (-1/4\pi\omega^2)[(\omega/c)^2\overline{\mathbf{I}} + \nabla\nabla]\cdot e^{i(\omega/c)|\mathbf{x}-\mathbf{x}'|}/|\mathbf{x}-\mathbf{x}'|$. The Fourier coefficient is related to the position- and frequency-dependent field, evaluated at $\mathbf{x} = (\mathbf{x}_{n\kappa}, z = 0)$ and $\omega = \varepsilon_{if}$, as $\mathbf{E}^0_{fi}(\mathbf{x}_{n\kappa},\varepsilon_{if}) \equiv \mathbf{E}^0_{fi,\mathbf{q}\kappa}e^{i\mathbf{q}\cdot\mathbf{x}_n}$. Intrinsic excitations of the sample are encoded within the tensor-valued $\mathbf{q}$-dependent response function $\overline{\mathbf{\Pi}}_{\mathbf{q}\kappa\kappa'}(\varepsilon_{if})$, while the subset that are excited by the electron probe are characterized by the induced moment $\mathbf{p}_{n0,\mathbf{q}\kappa}(\varepsilon_{if}) = \sum_{\kappa'}\overline{\Pi}_{\mathbf{q}\kappa\kappa'}(\varepsilon_{if})\cdot\mathbf{E}^0_{fi,\mathbf{q}\kappa'}(\varepsilon_{if})$.

The discrete translation symmetry shared by each structure necessitates periodic energy-momentum dispersion of both phonon and LPP quasiparticle excitations. In either class of 2D material, Bloch wave excitations with in-plane momentum $\hbar\mathbf{K}$ can be described by the equations of motion (Supporting Information)

$$-\omega^2\mathbf{u}_{\mathbf{K}\kappa} - i\eta\omega\mathbf{u}_{\mathbf{K}\kappa} + \sum_{\kappa'}\overline{\mathcal{D}}_{\kappa\kappa'}(\mathbf{K},\omega)\cdot\mathbf{u}_{\mathbf{K}\kappa'} = Z_\kappa e M_\kappa^{-1}\mathbf{E}^0_{\mathbf{K}\kappa} \tag{4}$$

where the displacement of the coordinate at lattice position $\mathbf{x}_{n\kappa}$ is $\mathbf{u}_{n\kappa} = \mathbf{u}_{\mathbf{K}\kappa}e^{i\mathbf{K}\cdot\mathbf{x}_n}e^{-i\omega t}$. Electron beams serve as one example of a probe of reciprocal space lattice excitations, where the in-plane recoil momentum $\hbar\mathbf{q}_\parallel$ is the Bloch momentum $\hbar\mathbf{K}$. However, propagating free space light can also drive lattice responses at specific $\mathbf{K}$ points corresponding to the projection $\mathbf{k}_\parallel$ of its wavevector $\mathbf{k}$ onto the sample plane. In either case, the induced moments are $\mathbf{p}_{n0,\mathbf{K}} = [Z_1e\mathbf{u}_{K1}, ..., Z_se\mathbf{u}_{\mathbf{K}s}] = [(-\omega^2 - i\eta\omega)\overline{\overline{\mathbf{I}}} + \overline{\overline{\mathcal{D}}}(\mathbf{K},\omega)]^{-1}[(Z_1e)^2\mathbf{E}^0_{\mathbf{K}1}/M_1, ..., (Z_se)^2\mathbf{E}^0_{\mathbf{K}s}/M_s] = \overline{\overline{\mathbf{\Pi}}}_{\mathbf{K}}(\omega)\mathbf{E}^0_{\mathbf{K}}$, where the $3s \times 1$ vector $\mathbf{E}^0_{\mathbf{K}} = [\mathbf{E}^0_{\mathbf{K}1}, ..., \mathbf{E}^0_{\mathbf{K}s}]$ represents the specific probe under consideration evaluated at each of the s sublattice sites. Double bars have been introduced to distinguish $3s \times 3s$ matrices from 3×3 matrices, which have a single bar, e.g., $[\overline{\overline{\mathbf{\Pi}}}_{\mathbf{K}}(\omega)]_{\kappa\kappa'} = \overline{\mathbf{\Pi}}_{\mathbf{K}\kappa\kappa'}(\omega)$, while the absence of a κ subscript indicates that a vector is $3s \times 1$.

Focusing first on atomic crystal phonons where the resonant IR wavelengths together with subnanometer bond lengths justify neglect of the finite speed of light, the generalized dynamical matrix $\overline{\mathcal{D}}_{\kappa\kappa'}(\mathbf{K},\omega)$ reduces to the conventional dynamical matrix $\overline{\mathbf{D}}_{\kappa\kappa'}(\mathbf{K}) = \overline{\mathbf{F}}_{\kappa\kappa'}(\mathbf{K}) + \overline{\mathbf{C}}_{\kappa\kappa'}(\mathbf{K})$,[79] which accounts for the sum of covalent $\overline{\mathbf{F}}_{\kappa\kappa'}(\mathbf{K})$ and ionic $\overline{\mathbf{C}}_{\kappa\kappa'}(\mathbf{K})$ interactions (Supporting Information). We compute all electron-induced graphene excitations within the harmonic crystal approximation[79,80] based upon eq 4 using an empirically parametrized model[81,82] for $\overline{\mathbf{F}}_{\kappa\kappa'}(\mathbf{q}_\parallel)$ and $\mathbf{q}$-dependent effective charges $Z_\kappa(\mathbf{q}_\parallel)$ along Γ−M from ref 26 (Supporting Information). Within the sample and scattering planes lie the longitudinal acoustic (LA) and optical (LO) phonons, while the transverse acoustic (TA) and optical (TO) phonons are polarized within the sample plane but are oriented perpendicular to the scattering plane. Oscillations of the z-directed acoustic (ZA) and optical (ZO) phonons are directed normal to the sample plane. Figures 2a,b display the calculated energy-momentum dispersion $\hbar\omega_\lambda(\mathbf{K}')$ of the phonon eigenmodes (gray traces), where $\lambda = 1-6$ denotes the band indices, as well as the phononic responses induced under wide-field (plane-wave) electron excitation as encoded in the q-EELS DDCS collected in the transmission (panel a) and reflection (panel b) geometries, where momentum conservation requires $\mathbf{K} = \mathbf{q}_\parallel = (\mathbf{q}\cdot\hat{\mathbf{x}})\hat{\mathbf{x}} = \mathbf{K}' + \mathbf{G}$, with $\mathbf{G}$ a reciprocal lattice vector. At each $\mathbf{q}_\parallel$ point, the spectrum is independently normalized to the maximum DDCS value, as in ref 26. For unnormalized q-EELS DDCS spectra, see Figure S1. In Figure 2a, the incident plane-wave wave vector $\mathbf{k}_i$ of the electron probe is normal to the graphene surface ($\theta_i = 0°$), and its initial speed is $v_i = 0.3c$, which are parameters typical of q-EELS experiments performed in the transmission geometry.[17,26] Reflection measurements, on the other hand, generally involve momentum transfers with a larger out-of-plane component (Figures 1a,b) such that the DDCS is largest for low incident electron kinetic energies and large angles of incidence θ_i.[23−25] Thus, for the reflection calculations in Figure 2b, we choose $\theta_i = 80°$ from the surface normal and $v_i = 0.01c$, which is typical of HREELS experiments.

It is evident from eq 2 that the selection rule for electron beam excitation of a specific phonon mode $\boldsymbol{\xi}_\lambda$ at $\mathbf{q}_\parallel$ of energy $\hbar\varepsilon_{if}$ requires overlap of the electron's vacuum field $\mathbf{E}^{0*}_{fi,\mathbf{q}}$ in eq 3 with the induced phonon moment $\mathbf{p}_{n0}$ dominated by $\boldsymbol{\xi}_\lambda$ at $\mathbf{q}_\parallel$ and $\hbar\varepsilon_{if}$. However, in the quasi-static ($c \to \infty$) and dipole ($a \ll 2\pi c/\varepsilon_{if}$) limits relevant to graphene, the electron's transition field $\mathbf{E}^0_{fi,\mathbf{q}}(\mathbf{x}) \propto q^{-2}\mathbf{q}$, and the general induced phonon moments become the induced dipole moments, i.e., $\mathbf{p}_{n0} \to \mathbf{d}_{n0}$, so that the selection rule $\mathbf{E}^{0*}_{fi,\mathbf{q}}\cdot\mathbf{p}_{n0,\mathbf{q}}$ reduces to $\sum_\kappa\mathbf{q}\cdot\mathbf{d}_{n0,\mathbf{q}\kappa} = \sum_\kappa\mathbf{q}_\parallel\cdot\mathbf{d}^\parallel_{n0,\mathbf{q}\kappa} + q_z d^z_{n0,\mathbf{q}\kappa}$. Based upon the dipole limit of the scattering form factor of a single Coulombically bound target electron, $\langle n|e^{i\mathbf{q}\cdot\mathbf{x}}|0\rangle \approx \langle n|1 + i\mathbf{q}\cdot\mathbf{x} + \cdots|0\rangle \propto \mathbf{q}\cdot\mathbf{d}_{n0}$,[83] this result is expected as electromagnetic retardation effects are negligible for graphene. The $\sum_\kappa\mathbf{q}\cdot\mathbf{d}_{n0,\mathbf{q}\kappa}$ selection rule is also related to that invoked to rationalize HREELS and q-EELS phonon measurements.[26,84,85]

While the $\sum_\kappa\mathbf{q}\cdot\mathbf{d}_{n0,\mathbf{q}\kappa}$ selection rule explains the absence of the TO and TA bands in the spectra presented in Figure 2 on grounds of symmetry, the degree to which accessible bands contribute to the DDCS spectra inside (and outside) the first BZ can be more clearly understood by considering the top line of eq 2. In particular, the DDCS is proportional to $|\mathbf{E}^0_{fi,\mathbf{q}}|^2\,\mathrm{Im}[\hat{\mathbf{E}}^{0*}_{fi,\mathbf{q}}\cdot\overline{\overline{\mathbf{\Pi}}}_{\mathbf{q}}\cdot\hat{\mathbf{E}}^0_{fi,\mathbf{q}}]$, showing that the characteristics of the transition field largely dictate how strongly each tensor component of $\overline{\overline{\mathbf{\Pi}}}_{\mathbf{q}}$ contributes to the DDCS. Although the eigenmode dispersion is periodic in reciprocal space, the momentum dependence of the effective charges $Z_\kappa(\mathbf{q})$ causes $\overline{\overline{\mathbf{\Pi}}}_{\mathbf{K}'+\mathbf{G}} \neq \overline{\overline{\mathbf{\Pi}}}_{\mathbf{K}'}$. The dispersions in $\mathbf{q}_\parallel$ of the electron's field $\mathbf{E}^0_{fi}$ (solid red/blue traces) as well as that of its limiting quasi-static form $\mathbf{E}^0_{fi} \propto \mathbf{q}$ (dotted red/blue traces) are displayed in Figures 2c,d for both transmission and reflection geometries, clearly showing the reduction of the former to the latter in the quasi-static limit appropriate to graphene. Notably, in transmission, the probe is strongly x-polarized except in the immediate vicinity of Γ_0, explaining the preferential excitation of both LA and LO phonons at both small and large momenta, as recently observed in q-EELS measurements of individual freestanding graphene monolayers.[26]

In contrast, the probe's polarization in the reflection geometry (Figure 2d) evolves from predominantly z-polarized in the first BZ to predominantly x-polarized in the second BZ. This crossover in polarization content of the electron's field elucidates the computed DDCS in Figure 2b, where primary excitation of ZA and ZO phonons at low momenta[23,24] give way to the additional excitation of both LA and LO phonons outside of the first BZ. Taken together, these results contrast the different information contained within q-EELS and

https://doi.org/10.1021/acs.nanolett.4c01797
Nano Lett. 2024, 24, 7748−7756

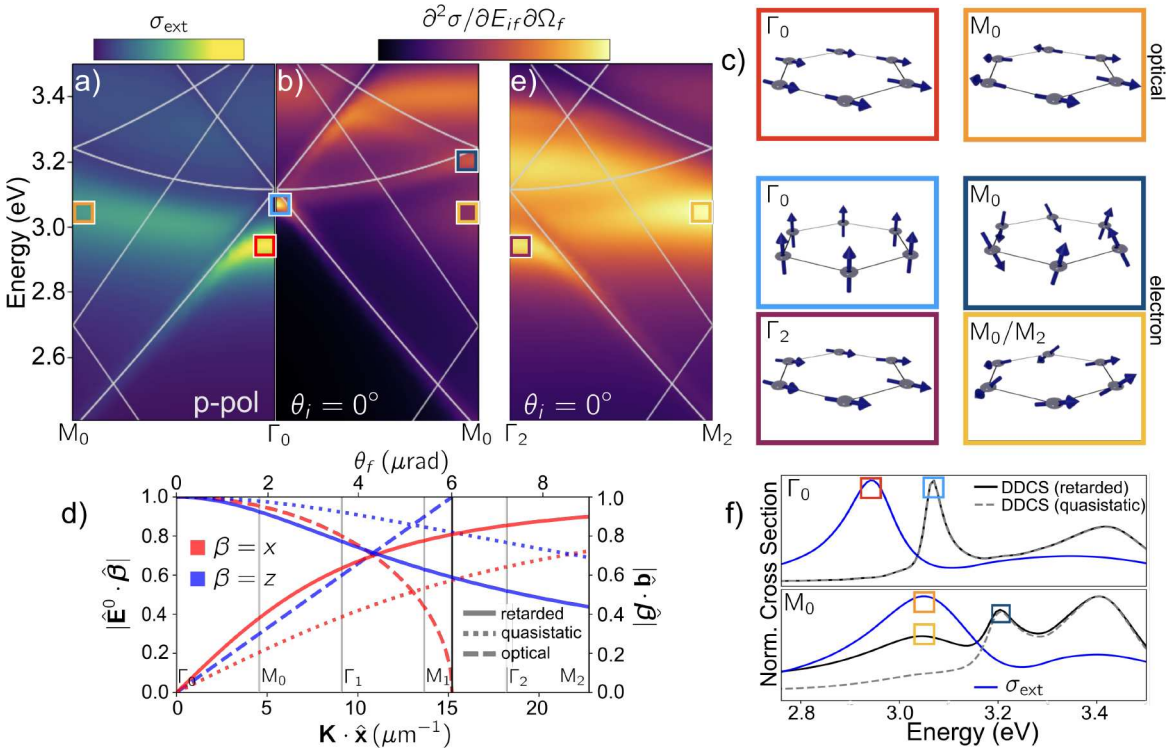

Figure 3. Energy-momentum dispersion of LPPs along the Γ−M direction in a honeycomb plasmonic array composed of 100 nm wide × 60 nm high silver nanodisks separated by 460 nm. The localized surface plasmon energies of each isolated nanodisk are 3.13 and 3.36 eV in the x and z directions, respectively. (a) Normalized optical extinction cross section under p-polarized excitation as a function of incident wave vector $\mathbf{k}_{\parallel}$ in the first BZ. (b) Normalized q-EELS DDCS calculated in the transmission geometry versus recoil wave vector $\mathbf{q}_{\parallel}$ in the first BZ. The electron's incident wave vector $\mathbf{k}_i$ is oriented normal to the sample surface with an initial velocity of $v_i = 0.7c$. (c) Induced LPP polarizations extracted at the boxed points in the optical extinction and q-EELS DDCS spectra. (d) Polarization dispersion of the electron's vacuum transition field $\mathbf{E}^0_{fi}$ (solid red/blue) and of the free space plane wave optical field $\mathbf{E}^0$ (dashed red/blue) contrasted against that of the electron's vacuum field $\mathbf{E}^0_{fi} \propto \mathbf{q}$ in the quasi-static limit (dotted red/blue) along the Γ_0−M_2 direction, all computed at 3 eV. The black vertical line indicates the light cone boundary corresponding to an optical excitation angle of 90° with respect to the surface normal. (e) q-EELS DDCS under the same conditions as (b) along Γ_2−M_2. The white traces in (a), (b), and (e) are the photonic dispersion of the empty honeycomb lattice. (f) Normalized momentum-resolved extinction (blue traces) and retarded/quasi-static DDCS spectra (black/gray-dashed traces) at Γ_0 and M_0 points from (a) and (b). All calculations used a vacuum background.

HREELS measurements of graphene performed at IR energies in the first two BZs. For comparison, optical excitation via propagating free space light is strongly limited in the IR by the light cone boundary, where $\mathbf{K} = |\mathbf{k}|\hat{\mathbf{x}} \sim 10^{-3}$ nm^{-1} (see dashed red/blue traces in the inset of Figure 2c).

Sharing the same hexagonal lattice structure as graphene but with a lattice constant of a = 460 nm,Figure 3 considers a 2D plasmonic honeycomb array composed of 100 nm diameter × 60 nm high silver nanodisks. In contrast to graphene, the large lattice constant and optical excitation frequencies of the array renders the entire BZ accessible to optical excitation.[48] Displayed in Figure 3a is the angle-resolved optical extinction cross section $\sigma_{ext}(\mathbf{k},\omega) = (4\pi\omega/c)\ \mathrm{Im}[\sum_{\kappa}\mathbf{E}^{0*}_{\mathbf{k}\kappa}\cdot\mathbf{p}_{n0,\mathbf{k}\kappa}/|\mathbf{E}^0_{\mathbf{k}\kappa}|^2]$, where $\mathbf{E}^0_{\mathbf{k}\kappa} = E_0\hat{\boldsymbol{\epsilon}}(\mathbf{k})e^{i\mathbf{k}\cdot\mathbf{r}_\kappa}$ is the Fourier coefficient of the stimulating optical plane-wave field with wave vector $\mathbf{k}$, while the fully retarded q-EELS DDCS (eq 2) is shown in Figure 3b, both within the first BZ. The inelastic electron scattering spectra are computed in the forward scattering geometry with $\mathbf{k}_i$ oriented along the z-axis ($\theta_i = 0°$) and $v_i = 0.7c$. Both optical and electron beam LPP spectra are calculated from eq 4 using the method of coupled dipoles where the multipolar plasmon moments $\mathbf{p}_{n0}$ in each silver nanodisk are approximated by individual point electric dipole moments $\mathbf{d}_{n0}$[86,87] with anisotropic polarizability evaluated using tabulated dielectric data for silver[88] (Supporting Information). Unlike for graphene, site-to-site coupling in nanoparticle arrays is mediated by long-range, causal interactions between nano-photonic antenna modes localized to each nanoscale scattering element. As a consequence,the generalized dynamical matrix $\bar{\mathcal{D}}_{\kappa\kappa'}(\mathbf{K},\omega)$ for LPPs encodes the individual nanoantenna resonances as well as the retarded dipole−dipole interactions between sites (Supporting Information). The white traces in Figures 3a,b denote the empty lattice photon dispersion in the reduced zone scheme.[89]

The honeycomb lattice LPPs are photonic analogues of the acoustic (in-phase) and optical (out-of-phase) transverse (TA, TO), longitudinal (LA, LO), and z-directed (ZA, ZO) phonon modes of graphene. Under p-polarization, optical extinction (Figure 3a) reveals the in-plane (x-polarized) in-phase LPP at Γ_0, while the electron DDCS (Figure 3b) probes the complementary out-of-plane (z-polarized) in-phase LPP at the same reciprocal space point, as seen by the color-coded induced moment plots in Figure 3c. The induced dipoles exhibit the expected in-phase and out-of-phase polarizations between sites within the unit cell at the high-symmetry points shown in Figures 3a,b. The complementary behavior exhibited by photon and electron probes in Figures 3a,b is generic and can again be understood by examining the general dispersion

https://doi.org/10.1021/acs.nanolett.4c01797
Nano Lett. 2024, 24, 7748−7756

of the electron's vacuum transition field $\mathbf{E}^0_{fi}$ (solid blue/red traces) versus that of plane-wave light $\mathbf{E}^0$ (dashed blue/red traces) shown in Figure 3d. In moving from the first to second BZ, the p-polarized optical field $\mathbf{E}^0$ switches from dominantly x-polarized to dominantly z-polarized at the light cone edge near M_1, while $\mathbf{E}^0_{fi}$ from eq 3 is predominantly polarized in the z direction in the first BZ but evolves to be largely x-polarized at larger $\mathbf{K} = \mathbf{q}_\parallel$. Indeed the computed optical extinction spectrum in Figure 3a shows clear signatures of the x-polarized in-phase and out-of-phase LPPs with increasing $\mathbf{k}_\parallel$ in the first BZ. Near the light cone edge, the z-polarized in-phase LPP becomes evident in $\sigma_{ext}(\mathbf{k},\omega)$; however, the z-polarized out-of-phase LPP is not apparent (Figure S2a). The evolution of $\sigma_{ext}(\mathbf{k},\omega)$ under s- and p-polarized excitation as $\mathbf{k}_\parallel$ traverses the full boundary of the irreducible BZ is shown in Figure S3a,b. Oppositely, but reflecting the crossover behavior in $\mathbf{E}^0_{fi}$ polarization at larger $\mathbf{q}_\parallel$ values in Figure 3d, the electron probe excites primarily the z-polarized out-of-phase LPP at M_0 as well as both x-polarized out-of-phase and in-phase LPPs at M_0/M_2 and Γ_2, respectively, in the third BZ (Figure 3e), a region inaccessible to free space optical excitation. The $\mathbf{q}_\parallel$ value where x- and z-polarized $\mathbf{E}^0_{fi}$ cross over can be tuned across multiple BZs in the transmission geometry by varying the primary kinetic energy of the probing electron (Figure S4). In the reflection geometry typical of HREELS, and as opposed to optical excitation, the electron's transition field is strongly z-polarized across many BZs (Figure S5).

In contrast to the near indistinguishability of quasi-static and fully retarded transition fields under the conditions presented in Figures 2c,d for graphene, Figure 3d displays noticeable differences in $\mathbf{E}^0_{fi}$ arising from the finite speed of light. The consequences of these differences are evident in Figure 3f, which displays normalized momentum-resolved optical (blue traces) and electron beam spectra at Γ_0 and M_0, where both fully retarded (black traces) and quasi-static (dashed gray traces) descriptions of the electron's vacuum transition field are adopted. While the normalized DDCS spectra are indistinguishable at the Γ_0 point, where the quasi-static and fully retarded fields in Figure 3d coincide, it is evident from the M_0 point spectra that a quasi-static description of the electron's field fails to fully capture the electron's ability to excite the x-polarized out-of-phase LPP in the first BZ at ∼3.05 eV. As compared to the quasi-static case, a fully retarded description of the electron's field involves a larger ratio of x- to z-polarized $\mathbf{E}^0_{fi}$ components, leading to stronger excitation of the x-polarized out-of-phase LPP. This differing evolution of the probe polarization with increasing $\mathbf{q}_\parallel$ and resulting complementarity in selection rules in comparison to optical excitation is generic to wide-field inelastic electron scattering processes involving any nanophotonic 2D periodic material.

While of considerable utility in the investigation of 2D atomic materials, spectroscopies derived from the inelastic scattering of wide-field free electron beams have found less consideration as probes of 2D periodic nanostructures. Here, we have presented a fully retarded theoretical approach to describe the low-energy inelastic scattering of wide-field electron beams from 2D periodic materials spanning from atomic-scale quantum materials to nanophotonic array structures beyond the nonrecoil approximation. Through inclusion of the relativistic kinematics appropriate to the forward and reflection geometries typical of q-EELS and HREELS measurements, we have investigated the reciprocal-space excitations native to a plasmonic honeycomb lattice under both inelastic electron scattering and angle-resolved optical extinction spectroscopies and compared these observables to the momentum-resolved phonon excitation spectrum of monolayer graphene. Generically, we find that important differences arise in the selection rules between 2D atomic and nanophotonic materials under optical- and electron-based probes, leading to complementary behavior in their polarization-dependent responses both inside and outside of the BZ. These differences, together with a breakdown of the quasi-static approximation, thus require consideration of fully retarded light−matter interactions and expanded selection rules to properly interpret inelastic electron scattering signals from 2D periodic materials. Beyond the examples highlighted, the presented theory might be utilized to investigate other material excitations[31,90−93] with symmetry selection based on free electron wavefront shaping.[77,78,94]

■ ASSOCIATED CONTENT

Supporting Information

The Supporting Information is available free of charge at https://pubs.acs.org/doi/10.1021/acs.nanolett.4c01797.

Additional details related to the employed graphene phonon model, two-dimensional lattice plasmon−polariton response matrix, additional graphene and lattice plasmon dispersion diagrams, and the incident electron speed dependence of the transition field (PDF)

■ AUTHOR INFORMATION

Corresponding Author

David J. Masiello − *Department of Chemistry, University of Washington, Seattle, Washington 98195, United States;* orcid.org/0000-0002-1187-0920; Email: masiello@uw.edu

Authors

Andrew W. Rossi − *Department of Chemistry, University of Washington, Seattle, Washington 98195, United States;* orcid.org/0000-0001-7588-534X

Marc R. Bourgeois − *Department of Chemistry, University of Washington, Seattle, Washington 98195, United States;* orcid.org/0000-0002-9435-9051

Caleb Walton − *Department of Chemistry, University of Washington, Seattle, Washington 98195, United States;* orcid.org/0009-0002-9543-6829

Complete contact information is available at: https://pubs.acs.org/10.1021/acs.nanolett.4c01797

Author Contributions

A.W.R. and M.R.B. contributed equally to this work.

Notes

The authors declare no competing financial interest.

■ ACKNOWLEDGMENTS

All work was supported by the U.S. Department of Energy (DOE), Office of Science, Office of Basic Energy Sciences (BES), Materials Sciences and Engineering Division, under Award No. DOE BES DE-SC0022921.

■ REFERENCES

(1) Hamers, R. Atomic-resolution surface spectroscopy with the scanning tunneling microscope. *Annu. Rev. Phys. Chem.* **1989**, *40*, 531−559.

(2) Saldin, D.; De Andres, P. Holographic LEED. *Phys. Rev. Lett.* **1990**, *64*, 1270.
(3) Bauer, E. Low energy electron microscopy. *Rep. Prog. Phys.* **1994**, *57*, 895.
(4) Wolkow, R. A. Direct observation of an increase in buckled dimers on Si(001) at low temperature. *Phys. Rev. Lett.* **1992**, *68*, 2636.
(5) Politano, A.; Marino, A. R.; Chiarello, G. Phonon dispersion of quasi-freestanding graphene on Pt(111). *J. Phys.-Condens. Mater.* **2012**, *24*, 104025.
(6) Endlich, M.; Miranda, H. P. C.; Molina-Sánchez, A.; Wirtz, L.; Kröger, J. Moiré-induced replica of graphene phonons on Ir(111). *Ann. Phys.* **2014**, *526*, 372−380.
(7) Siebentritt, S.; Pues, R.; Rieder, K.-H.; Shikin, A. M. Surface phonon dispersion in graphite and in a lanthanum graphite intercalation compound. *Phys. Rev. B* **1997**, *55*, 7927.
(8) Aizawa, T.; Souda, R.; Otani, S.; Ishizawa, Y.; Oshima, C. Anomalous bond of monolayer graphite on transition-metal carbide surfaces. *Phys. Rev. Lett.* **1990**, *64*, 768.
(9) Moresco, F.; Rocca, M.; Hildebrandt, T.; Henzler, M. Plasmon confinement in ultrathin continuous Ag films. *Phys. Rev. Lett.* **1999**, *83*, 2238.
(10) Petek, H.; Ogawa, S. Femtosecond time-resolved two-photon photoemission studies of electron dynamics in metals. *Prog. Surf. Sci.* **1997**, *56*, 239−310.
(11) Diaconescu, B.; Pohl, K.; Vattuone, L.; Savio, L.; Hofmann, P.; Silkin, V. M.; Pitarke, J. M.; Chulkov, E. V.; Echenique, P. M.; Farías, D.; Rocca, M. Low-energy acoustic plasmons at metal surfaces. *Nature* **2007**, *448*, 57−59.
(12) Bostwick, A.; Ohta, T.; Seyller, T.; Horn, K.; Rotenberg, E. Quasiparticle dynamics in graphene. *Nat. Phys.* **2007**, *3*, 36−40.
(13) Novoselov, K. S.; Geim, A. K.; Morozov, S. V.; Jiang, D.-e.; Zhang, Y.; Dubonos, S. V.; Grigorieva, I. V.; Firsov, A. A. Electric field effect in atomically thin carbon films. *Science* **2004**, *306*, 666−669.
(14) Novoselov, K. S.; Jiang, D.; Schedin, F.; Booth, T.; Khotkevich, V.; Morozov, S.; Geim, A. K. Two-dimensional atomic crystals. *Proc. Natl. Acad. Sci. U. S. A.* **2005**, *102*, 10451−10453.
(15) Naguib, M.; Kurtoglu, M.; Presser, V.; Lu, J.; Niu, J.; Heon, M.; Hultman, L.; Gogotsi, Y.; Barsoum, M. W. Two-dimensional nanocrystals produced by exfoliation of Ti_3AlC_2. *Adv. Mater.* **2011**, *23*, 4248−4253.
(16) Liu, H.; Neal, A. T.; Zhu, Z.; Luo, Z.; Xu, X.; Tománek, D.; Ye, P. D. Phosphorene: an unexplored 2D semiconductor with a high hole mobility. *ACS Nano* **2014**, *8*, 4033−4041.
(17) Hong, J.; Senga, R.; Pichler, T.; Suenaga, K. Probing exciton dispersions of freestanding monolayer WSe_2 by momentum-resolved electron energy-loss spectroscopy. *Phys. Rev. Lett.* **2020**, *124*, 087401.
(18) Mak, K. F.; Shan, J. Photonics and optoelectronics of 2D semiconductor transition metal dichalcogenides. *Nat. Photonics* **2016**, *10*, 216−226.
(19) Ross, J. S.; Wu, S.; Yu, H.; Ghimire, N. J.; Jones, A. M.; Aivazian, G.; Yan, J.; Mandrus, D. G.; Xiao, D.; Yao, W.; Xu, X. Electrical control of neutral and charged excitons in a monolayer semiconductor. *Nat. Commun.* **2013**, *4*, 1474.
(20) Kogar, A.; Rak, M. S.; Vig, S.; Husain, A. A.; Flicker, F.; Joe, Y. I.; Venema, L.; MacDougall, G. J.; Chiang, T. C.; Fradkin, E.; van Wezel, J.; Abbamonte, P. Signatures of exciton condensation in a transition metal dichalcogenide. *Science* **2017**, *358*, 1314−1317.
(21) Maultzsch, J.; Reich, S.; Thomsen, C.; Requardt, H.; Ordejón, P. Phonon dispersion in graphite. *Phys. Rev. Lett.* **2004**, *92*, 075501.
(22) Mohr, M.; Maultzsch, J.; Dobardžić, E.; Reich, S.; Milošević, I.; Damnjanović, M.; Bosak, A.; Krisch, M.; Thomsen, C. Phonon dispersion of graphite by inelastic x-ray scattering. *Phys. Rev. B* **2007**, *76*, 035439.
(23) Politano, A.; de Juan, F.; Chiarello, G.; Fertig, H. A. Emergence of an out-of-plane optical phonon (ZO) Kohn anomaly in quasifreestanding epitaxial graphene. *Phys. Rev. Lett.* **2015**, *115*, 075504.
(24) Politano, A. Spectroscopic investigations of phonons in epitaxial graphene. *Crit. Rev. Solid State* **2017**, *42*, 99−128.
(25) Li, J.; Li, J.; Tang, J.; Tao, Z.; Xue, S.; Liu, J.; Peng, H.; Chen, X.-Q.; Guo, J.; Zhu, X. Direct observation of topological phonons in graphene. *Phys. Rev. Lett.* **2023**, *131*, 116602.
(26) Senga, R.; Suenaga, K.; Barone, P.; Morishita, S.; Mauri, F.; Pichler, T. Position and momentum mapping of vibrations in graphene nanostructures. *Nature* **2019**, *573*, 247−250.
(27) Kramberger, C.; Hambach, R.; Giorgetti, C.; Rümmeli, M. H.; Knupfer, M.; Fink, J.; Büchner, B.; Reining, L.; Einarsson, E.; Maruyama, S.; Sottile, F.; Hannewald, K.; Olevano, V.; Marinopoulos, A. G.; Pichler, T. Linear plasmon dispersion in single-wall carbon nanotubes and the collective excitation spectrum of graphene. *Phys. Rev. Lett.* **2008**, *100*, 196803.
(28) Chen, J.; Badioli, M.; Alonso-González, P.; Thongrattanasiri, S.; Huth, F.; Osmond, J.; Spasenović, M.; Centeno, A.; Pesquera, A.; Godignon, P.; Zurutuza Elorza, A.; Camara, N.; de Abajo, F. J. G.; Hillenbrand, R.; Koppens, F. H. L. Optical nano-imaging of gate-tunable graphene plasmons. *Nature* **2012**, *487*, 77−81.
(29) Ni, G. X.; McLeod, A. S.; Sun, Z.; Wang, L.; Xiong, L.; Post, K. W.; Sunku, S. S.; Jiang, B.-Y.; Hone, J.; Dean, C. R.; Fogler, M. M.; Basov, D. N. Fundamental limits to graphene plasmonics. *Nature* **2018**, *557*, 530−533.
(30) Zhou, W.; Lee, J.; Nanda, J.; Pantelides, S. T.; Pennycook, S. J.; Idrobo, J.-C. Atomically localized plasmon enhancement in monolayer graphene. *Nat. Nanotechnol.* **2012**, *7*, 161−165.
(31) Husain, A. A.; Huang, E. W.; Mitrano, M.; Rak, M. S.; Rubeck, S. I.; Guo, X.; Yang, H.; Sow, C.; Maeno, Y.; Uchoa, B.; Chiang, T. C.; Batson, P. E.; Phillips, P. W.; Abbamonte, P. Pines' demon observed as a 3D acoustic plasmon in Sr_2RuO_4. *Nature* **2023**, *621*, 66−70.
(32) Politano, A.; Silkin, V. M.; Nechaev, I. A.; Vitiello, M. S.; Viti, L.; Aliev, Z. S.; Babanly, M. B.; Chiarello, G.; Echenique, P. M.; Chulkov, E. V. Interplay of Surface and Dirac Plasmons in Topological Insulators: The Case of Bi_2Se_3. *Phys. Rev. Lett.* **2015**, *115*, 216802.
(33) Kogar, A.; Vig, S.; Thaler, A.; Wong, M. H.; Xiao, Y.; Reig-i Plessis, D.; Cho, G. Y.; Valla, T.; Pan, Z.; Schneeloch, J.; Zhong, R.; Gu, G. D.; Hughes, T. L.; MacDougall, G. J.; Chiang, T.-C.; Abbamonte, P. Surface Collective Modes in the Topological Insulators Bi_2Se_3 and $Bi_{0.5}Sb_{1.5}Te_{3-x}Se_x$. *Phys. Rev. Lett.* **2015**, *115*, 257402.
(34) Politano, A.; Chiarello, G.; Ghosh, B.; Sadhukhan, K.; Kuo, C.-N.; Lue, C. S.; Pellegrini, V.; Agarwal, A. 3D Dirac Plasmons in the Type-II Dirac Semimetal $PtTe_2$. *Phys. Rev. Lett.* **2018**, *121*, 086804.
(35) Xue, S.; Wang, M.; Li, Y.; Zhang, S.; Jia, X.; Zhou, J.; Shi, Y.; Zhu, X.; Yao, Y.; Guo, J. Observation of Nodal-Line Plasmons in ZrSiS. *Phys. Rev. Lett.* **2021**, *127*, 186802.
(36) Liu, M.; Yin, X.; Ulin-Avila, E.; Geng, B.; Zentgraf, T.; Ju, L.; Wang, F.; Zhang, X. A graphene-based broadband optical modulator. *Nature* **2011**, *474*, 64−67.
(37) Bonaccorso, F.; Sun, Z.; Hasan, T.; Ferrari, A. Graphene photonics and optoelectronics. *Nat. Photonics* **2010**, *4*, 611−622.
(38) Liu, X.; Hersam, M. C. 2D materials for quantum information science. *Nat. Rev. Mater.* **2019**, *4*, 669−684.
(39) Krivanek, O. L.; Lovejoy, T. C.; Dellby, N.; Aoki, T.; Carpenter, R. W.; Rez, P.; Soignard, E.; Zhu, J.; Batson, P. E.; Lagos, M. J.; Egerton, R. F.; Crozier, P. A. Vibrational spectroscopy in the electron microscope. *Nature* **2014**, *514*, 209−212.
(40) Dwyer, C.; Aoki, T.; Rez, P.; Chang, S.; Lovejoy, T.; Krivanek, O. Electron-beam mapping of vibrational modes with nanometer spatial resolution. *Phys. Rev. Lett.* **2016**, *117*, 256101.
(41) Lagos, M. J.; Trügler, A.; Hohenester, U.; Batson, P. E. Mapping vibrational surface and bulk modes in a single nanocube. *Nature* **2017**, *543*, 529−532.
(42) Hage, F. S.; Nicholls, R. J.; Yates, J. R.; McCulloch, D. G.; Lovejoy, T. C.; Dellby, N.; Krivanek, O. L.; Refson, K.; Ramasse, Q. M. Nanoscale momentum-resolved vibrational spectroscopy. *Sci. Adv.* **2018**, *4*, eaar7495.
(43) Politano, A. On the fate of high-resolution electron energy loss spectroscopy (HREELS), a versatile probe to detect surface

https://doi.org/10.1021/acs.nanolett.4c01797
Nano Lett. 2024, 24, 7748−7756

excitations: Will the Phoenix rise again? *Phys. Chem. Chem. Phys.* **2021**, *23*, 26061−26069.
(44) Li, J.; Wang, L.; Wang, Y.; Tao, Z.; Zhong, W.; Su, Z.; Xue, S.; Miao, G.; Wang, W.; Peng, H.; Guo, J.; Zhu, X. Observation of the nonanalytic behavior of optical phonons in monolayer hexagonal boron nitride. *Nat. Commun.* **2024**, *15*, 1938.
(45) Vig, S.; Kogar, A.; Mitrano, M.; Husain, A. A.; Mishra, V.; Rak, M. S.; Venema, L.; Johnson, P. D.; Gu, G. D.; Fradkin, E.; Norman, M. R.; Abbamonte, P. Measurement of the dynamic charge response of materials using low-energy, momentum-resolved electron energy-loss spectroscopy (M-EELS). *SciPost Phys.* **2017**, *3*, 026.
(46) Yang, A.; Hoang, T. B.; Dridi, M.; Deeb, C.; Mikkelsen, M. H.; Schatz, G. C.; Odom, T. W. Real-time tunable lasing from plasmonic nanocavity arrays. *Nat. Commun.* **2015**, *6*, 6939.
(47) Guo, R.; Nečada, M.; Hakala, T. K.; Väkeväinen, A. I.; Törmä, P. Lasing at K Points of a Honeycomb Plasmonic Lattice. *Phys. Rev. Lett.* **2019**, *122*, 013901.
(48) Juarez, X. G.; Li, R.; Guan, J.; Reese, T.; Schaller, R. D.; Odom, T. W. M-point lasing in hexagonal and honeycomb plasmonic lattices. *ACS Photonics* **2022**, *9*, 52−58.
(49) Hirose, K.; Liang, Y.; Kurosaka, Y.; Watanabe, A.; Sugiyama, T.; Noda, S. Watt-class high-power, high-beam-quality photonic-crystal lasers. *Nat. Photonics* **2014**, *8*, 406−411.
(50) Zhen, B.; Hsu, C. W.; Lu, L.; Stone, A. D.; Soljačić, M. Topological nature of optical bound states in the continuum. *Phys. Rev. Lett.* **2014**, *113*, 257401.
(51) Azzam, S. I.; Shalaev, V. M.; Boltasseva, A.; Kildishev, A. V. Formation of bound states in the continuum in hybrid plasmonic-photonic systems. *Phys. Rev. Lett.* **2018**, *121*, 253901.
(52) Liang, Y.; Koshelev, K.; Zhang, F.; Lin, H.; Lin, S.; Wu, J.; Jia, B.; Kivshar, Y. Bound states in the continuum in anisotropic plasmonic metasurfaces. *Nano Lett.* **2020**, *20*, 6351−6356.
(53) Guan, J.; Sagar, L. K.; Li, R.; Wang, D.; Bappi, G.; Wang, W.; Watkins, N.; Bourgeois, M. R.; Levina, L.; Fan, F.; Hoogland, S.; Voznyy, O.; de Pina, J. M.; Schaller, R. D.; Schatz, G. C.; Sargent, E. H.; Odom, T. W. Quantum dot-plasmon lasing with controlled polarization patterns. *ACS Nano* **2020**, *14*, 3426−3433.
(54) Liang, Y.; Lin, H.; Lin, S.; Wu, J.; Li, W.; Meng, F.; Yang, Y.; Huang, X.; Jia, B.; Kivshar, Y. Hybrid anisotropic plasmonic metasurfaces with multiple resonances of focused light beams. *Nano Lett.* **2021**, *21*, 8917−8923.
(55) Ha, S. T.; Fu, Y. H.; Emani, N. K.; Pan, Z.; Bakker, R. M.; Paniagua-Domínguez, R.; Kuznetsov, A. I. Directional lasing in resonant semiconductor nanoantenna arrays. *Nat. Nanotechnol.* **2018**, *13*, 1042−1047.
(56) Mohamed, S.; Wang, J.; Rekola, H.; Heikkinen, J.; Asamoah, B.; Shi, L.; Hakala, T. K. Controlling topology and polarization state of lasing photonic bound states in continuum. *Laser Photonics Rev.* **2022**, *16*, 2100574.
(57) Liu, W.; Ji, Z.; Wang, Y.; Modi, G.; Hwang, M.; Zheng, B.; Sorger, V. J.; Pan, A.; Agarwal, R. Generation of helical topological exciton-polaritons. *Science* **2020**, *370*, 600−604.
(58) Bourgeois, M. R.; Beutler, E. K.; Khorasani, S.; Panek, N.; Masiello, D. J. Nanometer-scale spatial and spectral mapping of exciton polaritons in structured plasmonic cavities. *Phys. Rev. Lett.* **2022**, *128*, 197401.
(59) Chen, Y.; Miao, S.; Wang, T.; Zhong, D.; Saxena, A.; Chow, C.; Whitehead, J.; Gerace, D.; Xu, X.; Shi, S.-F.; Majumdar, A. Metasurface Integrated Monolayer Exciton Polariton. *Nano Lett.* **2020**, *20*, 5292−5300.
(60) Väkeväinen, A. I.; Moerland, R. J.; Rekola, H. T.; Eskelinen, A.-P.; Martikainen, J.-P.; Kim, D.-H.; Törmä, P. Plasmonic surface lattice resonances at the strong coupling regime. *Nano Lett.* **2014**, *14*, 1721−1727.
(61) Shi, L.; Hakala, T.; Rekola, H.; Martikainen, J.-P.; Moerland, R.; Törmä, P. Spatial coherence properties of organic molecules coupled to plasmonic surface lattice resonances in the weak and strong coupling regimes. *Phys. Rev. Lett.* **2014**, *112*, 153002.
(62) Baranov, D. G.; Wersall, M.; Cuadra, J.; Antosiewicz, T. J.; Shegai, T. Novel nanostructures and materials for strong light-matter interactions. *ACS Photonics* **2018**, *5*, 24−42.
(63) Hakala, T. K.; Moilanen, A. J.; Vakevainen, A. I.; Guo, R.; Martikainen, J.-P.; Daskalakis, K. S.; Rekola, H. T.; Julku, A.; Torma, P. Bose−Einstein Condensation in a Plasmonic Lattice. *Nat. Phys.* **2018**, *14*, 739−744.
(64) Berghuis, A. M.; Castellanos, G. W.; Murai, S.; Pura, J. L.; Abujetas, D. R.; van Heijst, E.; Ramezani, M.; Sánchez-Gil, J. A.; Rivas, J. G. Room Temperature Exciton-Polariton Condensation in Silicon Metasurfaces Emerging from Bound States in the Continuum. *Nano Lett.* **2023**, *23*, 5603−5609.
(65) Cherqui, C.; Bourgeois, M. R.; Wang, D.; Schatz, G. C. Plasmonic surface lattice resonances: theory and computation. *Acc. Chem. Res.* **2019**, *52*, 2548−2558.
(66) Baur, S.; Sanders, S.; Manjavacas, A. Hybridization of Lattice Resonances. *ACS Nano* **2018**, *12*, 1618−1629.
(67) Takeuchi, K.; Yamamoto, N. Visualization of surface plasmon polariton waves in two-dimensional plasmonic crystal by cathodoluminescence. *Opt. Express* **2011**, *19*, 12365−12374.
(68) Saito, H.; Yoshimoto, D.; Moritake, Y.; Matsukata, T.; Yamamoto, N.; Sannomiya, T. Valley-Polarized Plasmonic Edge Mode Visualized in the Near-Infrared Spectral Range. *Nano Lett.* **2021**, *21*, 6556−6562.
(69) Shekhar, P.; Malac, M.; Gaind, V.; Dalili, N.; Meldrum, A.; Jacob, Z. Momentum-resolved electron energy loss spectroscopy for mapping the photonic density of states. *ACS Photonics* **2017**, *4*, 1009−1014.
(70) Saito, H.; Lourenço-Martins, H.; Bonnet, N.; Li, X.; Lovejoy, T. C.; Dellby, N.; Stéphan, O.; Kociak, M.; Tizei, L. H. G. Emergence of point defect states in a plasmonic crystal. *Phys. Rev. B* **2019**, *100*, 245402.
(71) Batson, P. A new surface plasmon resonance in clusters of small aluminum spheres. *Ultramicroscopy* **1982**, *9*, 277−282.
(72) Nelayah, J.; Kociak, M.; Stéphan, O.; García de Abajo, F. J.; Tencé, M.; Henrard, L.; Taverna, D.; Pastoriza-Santos, I.; Liz-Marzán, L. M.; Colliex, C. Mapping surface plasmons on a single metallic nanoparticle. *Nat. Phys.* **2007**, *3*, 348−353.
(73) García de Abajo, F. J. Optical excitations in electron microscopy. *Rev. Mod. Phys.* **2010**, *82*, 209.
(74) Cherqui, C.; Thakkar, N.; Li, G.; Camden, J. P.; Masiello, D. J. Characterizing localized surface plasmons using electron energy-loss spectroscopy. *Annu. Rev. Phys. Chem.* **2016**, *67*, 331−357.
(75) Polman, A.; Kociak, M.; García de Abajo, F. J. Electron-beam spectroscopy for nanophotonics. *Nat. Mater.* **2019**, *18*, 1158−1171.
(76) Glauber, R. J.; Lewenstein, M. Quantum optics of dielectric media. *Phys. Rev. A* **1991**, *43*, 467.
(77) Bourgeois, M. R.; Nixon, A. G.; Chalifour, M.; Masiello, D. J. Optical polarization analogs in inelastic free-electron scattering. *Sci. Adv.* **2023**, *9*, eadj6038.
(78) Nixon, A. G.; Chalifour, M.; Bourgeois, M. R.; Sanchez, M.; Masiello, D. J. Inelastic scattering of transversely structured free electrons from nanophotonic targets: Theory and computation. *Phys. Rev. A* **2024**, *109*, 043502.
(79) Dove, M. T. *Introduction to Lattice Dynamics*; Cambridge University Press: 1993.
(80) Hohenester, U.; Trügler, A.; Batson, P. E.; Lagos, M. J. Inelastic vibrational bulk and surface losses of swift electrons in ionic nanostructures. *Phys. Rev. B* **2018**, *97*, 165418.
(81) Bosak, A.; Krisch, M.; Mohr, M.; Maultzsch, J.; Thomsen, C. Elasticity of single-crystalline graphite: Inelastic x-ray scattering study. *Phys. Rev. B* **2007**, *75*, 153408.
(82) Michel, K.; Verberck, B. Theory of the evolution of phonon spectra and elastic constants from graphene to graphite. *Phys. Rev. B* **2008**, *78*, 085424.
(83) Sakurai, J. J. *Modern Quantum Mechanics*; Benjamin/Cummings Publishing Company: 1985.
(84) de Juan, F.; Politano, A.; Chiarello, G.; Fertig, H. A. Symmetries and selection rules in the measurement of the phonon

https://doi.org/10.1021/acs.nanolett.4c01797
Nano Lett. 2024, 24, 7748−7756

spectrum of graphene and related materials. *Carbon* **2015**, *85*, 225−232.
(85) Nicholls, R.; Hage, F.; McCulloch, D.; Ramasse, Q.; Refson, K.; Yates, J. Theory of momentum-resolved phonon spectroscopy in the electron microscope. *Phys. Rev. B* **2019**, *99*, 094105.
(86) Bourgeois, M. R.; Rossi, A. W.; Chalifour, M.; Cherqui, C.; Masiello, D. J. Lattice Kerker effect with plasmonic oligomers. *J. Phys. Chem. C* **2021**, *125*, 18817−18826.
(87) Bourgeois, M. R.; Rossi, A. W.; Khorasani, S.; Masiello, D. J. Optical control over thermal distributions in topologically trivial and non-trivial plasmon lattices. *ACS Photonics* **2022**, *9*, 3656−3667.
(88) Johnson, P. B.; Christy, R. W. Optical constants of the noble metals. *Phys. Rev. B* **1972**, *6*, 4370−4379.
(89) Guo, R.; Hakala, T. K.; Törmä, P. Geometry dependence of surface lattice resonances in plasmonic nanoparticle arrays. *Phys. Rev. B* **2017**, *95*, 155423.
(90) Dai, Y.; Zhou, Z.; Ghosh, A.; Mong, R. S.; Kubo, A.; Huang, C.-B.; Petek, H. Plasmonic topological quasiparticle on the nanometre and femtosecond scales. *Nature* **2020**, *588*, 616−619.
(91) Davis, T. J.; Janoschka, D.; Dreher, P.; Frank, B.; Meyer zu Heringdorf, F.-J.; Giessen, H. Ultrafast vector imaging of plasmonic skyrmion dynamics with deep subwavelength resolution. *Science* **2020**, *368*, eaba6415.
(92) Zhang, L.; Niu, Q. Chiral phonons at high-symmetry points in monolayer hexagonal lattices. *Phys. Rev. Lett.* **2015**, *115*, 115502.
(93) Zhu, H.; Yi, J.; Li, M.-Y.; Xiao, J.; Zhang, L.; Yang, C.-W.; Kaindl, R. A.; Li, L.-J.; Wang, Y.; Zhang, X. Observation of chiral phonons. *Science* **2018**, *359*, 579−582.
(94) Lourenço-Martins, H.; Gérard, D.; Kociak, M. Optical polarization analogue in free electron beams. *Nat. Phys.* **2021**, *17*, 598−603.

https://doi.org/10.1021/acs.nanolett.4c01797
Nano Lett. 2024, 24, 7748−7756